

# Comparison of Near-Fault Displacement Interpretations from Field and Aerial Data for the M 6.5 and 7.1 Ridgecrest Earthquake Sequence Ruptures

Christine A. Goulet<sup>\*1</sup>, Yongfei Wang<sup>1</sup>, Chukwuebuka C. Nweke<sup>2</sup>, Bo-xiang Tang<sup>3</sup>, Pengfei Wang<sup>3</sup>, Kenneth S. Hudson<sup>3</sup>, Sean K. Ahdi<sup>4</sup>, Xiaofeng Meng<sup>1</sup>, Martin B. Hudson<sup>5</sup>, Andrea Donnellan<sup>6</sup>, Gregory A. Lyzenga<sup>6</sup>, Scott J. Brandenberg<sup>3</sup>, Jonathan P. Stewart<sup>3</sup>, Timu Gallien<sup>3</sup>, and Maria A. Winters<sup>3</sup>

## ABSTRACT

Coseismic surface fault displacement presents a serious potential hazard for structures and for lifeline infrastructure. Distributed lifeline infrastructure tends to cover large distances and may cross faults in multiple locations, especially in active tectonic regions like California. However, fault displacement measurements for engineering applications are quite sparse, rendering the development of predictive models extremely difficult and fraught with large uncertainties. Detailed fault surface rupture mapping products exist for a few documented cases, but they may not capture the full width of ground deformations that are likely to impact distributed infrastructure. The 2019 Ridgecrest earthquake sequence presented an ideal opportunity to collect data and evaluate the ability of different techniques to capture coseismic deformations on and near the fault ruptures. Both the M 6.5 and 7.1 events ruptured the surface in sparsely populated desert areas where little vegetation is present to obscure surficial features. Two study areas ( $\sim 400 \text{ m} \times 500 \text{ m}$  each) around the surface ruptures from the two events were selected. Teams of researchers were deployed and coordinated to gather data in three ways: field measurements and photographs, imagery from small uninhabited aerial systems, and imagery from airborne light detection and ranging. Each of these techniques requires different amounts of resources in terms of cost, labor, and time associated with the data collection, processing, and interpretation efforts. This article presents the data collection methods used for the two study areas, and qualitative and quantitative comparisons of the results interpretations. While all three techniques capture the key features that are important for displacement design of distributed infrastructure, the use of remote sensing methods in combination with field measurements presents an advantage over the use of any single technique.

## KEY POINTS

- Engineering infrastructure seismic design is often controlled by potential fault displacements.
- Accurate quantification of on- and off-fault displacements is needed for scientific and engineering modeling.
- Collection with cross-validation of displacement data from complementary methods (field and aerial) is ideal.

## Supplemental Material

## INTRODUCTION AND MOTIVATION

Surface fault rupture due to earthquakes may result in a serious hazard for structures and lifelines. Water conduits, gas and

- Southern California Earthquake Center, University of Southern California, Los Angeles, California, U.S.A., <https://orcid.org/0000-0002-7643-357X> (CAG); <https://orcid.org/0000-0003-1121-7726> (YW); <https://orcid.org/0000-0002-3750-6342> (XM); 2. Sonny Astani Department of Civil and Environmental Engineering, University of Southern California, Los Angeles, California, U.S.A.; 3. Department of Civil & Environmental Engineering, University of California, Los Angeles, California, U.S.A., <https://orcid.org/0000-0001-6006-8355> (KSH); <https://orcid.org/0000-0003-2493-592X> (SJB); <https://orcid.org/0000-0003-3602-3629> (JPS); <https://orcid.org/0000-0003-2905-1306> (TG); 4. Department of Earth, Planetary, & Space Sciences, University of California, Los Angeles, California, U.S.A., <https://orcid.org/0000-0003-0274-5180> (SKA); 5. Turner Engineering Group, Turner Construction Company, Los Angeles, California, U.S.A.; 6. Jet Propulsion Laboratory, California Institute of Technology, Pasadena, California, U.S.A., <https://orcid.org/0000-0001-6843-8373> (AD); <https://orcid.org/0000-0001-6792-1515> (GAL)

\*Corresponding author: cgoulet@usc.edu

**Cite this article as:** Goulet, C. A., Y. Wang, C. C. Nweke, B. Tang, P. Wang, K. S. Hudson, S. K. Ahdi, X. Meng, M. B. Hudson, A. Donnellan, et al. (2021). Comparison of Near-Fault Displacement Interpretations from Field and Aerial Data for the M 6.5 and 7.1 Ridgecrest Earthquake Sequence Ruptures, *Bull. Seismol. Soc. Am.* **XX**, 1–17, doi: [10.1785/0120200222](https://doi.org/10.1785/0120200222)

© Seismological Society of America

petroleum pipelines, electrical transmission lines, and roadways and rail systems are especially vulnerable to fault displacements due to their distributed nature. It is generally not possible to avoid all potentially active faults for long lifelines without significant cost-prohibitive mitigation measures. For the design of such systems, engineers make use of probabilistic fault displacement hazard analysis (PFDHA) models from which they determine expected displacement for a given earthquake scenario and/or for a given probability of occurrence. These PFDHA models (e.g., Stepp *et al.*, 2001; Youngs *et al.*, 2003; Moss and Ross, 2011; Petersen *et al.*, 2011) are usually developed by aggregating available fault displacement data and combining them with fault geometry and slip rates. Relative to semiempirical earthquake ground-motion models (also known as ground motion prediction equations), displacement models are few and poorly constrained, partly due to the lack of detailed fault displacement observations. Two of the coauthors of the present article are involved in the large multi-institution Fault Displacement Hazard Initiative (FDHI) ([Fault Displacement Hazard Initiative \[FDHI\], 2018](#)) aimed at developing PFDHA models. As part of this work, a fault displacement database has been developed and numerical simulations are being conducted to supplement sparse empirical data sets ([Wang and Goulet, 2021](#)). Engagement in the FDHI, which highlighted the data issues and needs, was the motivation for the study presented herein.

Surface displacements are highly perishable features that can be quickly disturbed by wind, rain, or even by “earthquake tourism” if relatively easily accessible to people. Data collection following earthquakes often prioritizes covering as much of the main fault rupture length as possible, which may lead to a deprioritization of off-fault field measurements. Traditionally, detailed displacement information has been difficult to collect in a comprehensive way so as to inform fault displacement models. The data sets are not always complete, and the data set completeness is sometimes difficult to determine from publications, a fact highlighted in recent large database building efforts (e.g., Sarmiento *et al.*, 2019; Baize *et al.*, 2020). For example, when there is no displacement data reported at a specific location, it is usually impossible to know if it was because there was zero displacement or because the site was not visited. Data limitations are especially pronounced for secondary features located off the main fault trace by tens to hundreds of meters. Such features seldom draw the attention of reconnaissance teams, and yet they may represent potentially significant engineering hazards to distributed infrastructure.

This issue was highlighted in Rockwell *et al.* (2002), who documented detailed mapping of sections of the fault ruptures from the 1999 Izmit and Duzce, Turkey, earthquakes, noting that part of the slip is missed if the focus is too narrowly defined in the fault-normal direction. Treiman *et al.* (2002) also noted shear distributions observed away from the Hector Mine earthquake fault trace. Although such features representing bends in the shallow sediments may not contribute largely to the total

observed slip, they may damage infrastructure. For example, small fault offsets distributed over tens of meters may not control the design of a buried ductile pipeline; however, such small offsets can be important for strain-sensitive infrastructure systems like high-speed rail. In the context of PFDHA development and use in design, data completeness along and across faults is critical for defining both the design quantities and their uncertainty.

The advent and availability of new technologies in the last few decades now provides the science and engineering communities with tools that can quantify surface rupture features more accurately. On-the-ground surveys and measurements are still critical, but surveys from small uninhabited aerial systems (sUAS, also known as drones) with onboard cameras can supplement those data at a relatively low cost. The advantage of using sUAS and other remote surveying systems is twofold: (1) they can cover a relatively large area in a short time; and (2) they can take images of regions that may be difficult to access by roads or on foot. The airborne light detection and ranging (lidar) technique can also be used to cover even broader areas, but tends to have a lower resolution and it is not as cost effective. New image data-processing techniques such as structure from motion (SfM) and Co-registration of Optically Sensed Images and Correlation are capable of capturing wide aperture displacements from aerial imagery ([Milliner \*et al.\*, 2015, 2016](#)), but these techniques are only useful if the imagery itself can capture what is actually in the field at an appropriate resolution. As useful as these techniques are, the fault displacements interpreted from aerial imagery can only be validated with the field data collected at the time, which may not be completely exhaustive, especially at distances away from the main fault strands. So, a new question arises: which method or combination of methods is most appropriate to collect perishable fault displacement data with the degree of resolution, aperture, and quality appropriate for hazard modeling?

The Ridgecrest earthquake sequence presented an opportunity to potentially answer this question and to design a study expressly for this purpose, involving multiple teams collecting complementary datasets over controlled study regions. The conditions in the California desert, with only limited vegetation, were ideal to study the strengths and weaknesses of several techniques. As part of a Geotechnical Extreme Events Reconnaissance (GEER) team mobilized to investigate the effects of this event sequence ([Geotechnical Extreme Events Reconnaissance \[GEER\], 2019](#)), data collected in the field was coordinated with different groups for sUAS and lidar surveys. The interpreted results allowed for a comparison of data collected across a variety of techniques, each involving a different level of field work and interpretation efforts. The comparison exercise was performed in limited overlapping areas around the moment magnitude M 6.5 and 7.1 ruptures (the study areas are discussed subsequently in more detail). Although the study areas are relatively small, they provided guidance on the validity of data that can only be accessed via remote imaging techniques. The rapid assessment and prioritization of data

collection techniques are especially important when earthquakes occur in remote regions or internationally where logistics may complicate reconnaissance activities.

An additional objective for the work was to collect a broad range of surface damage observations associated with faulting. Looking at the surface expression of faulting beyond displacement can provide data sets for the calibration of numerical damage models that go beyond plasticity (e.g., [Roten et al., 2017](#); [Wang and Goulet, 2021](#)) and that attempt to model the complete fault zone (e.g., [Sagy and Brodsky, 2009](#)) using more realistic physical models representing brittle failure (e.g., [Ashby and Sammis, 1990](#); [Thomas and Bhat, 2018](#)) or anchored in discrete element mechanics (e.g., [Cundall and Strack, 1979](#); [Benesh et al., 2007](#)). To this end, a surface expression categorization scheme and a digital dataset were developed.

This article presents the methodology underlying the study of both earthquakes, introduces a new nomenclature, and provides a data set documenting surface displacement features from thousands of field pictures following that nomenclature. The text presents the interpretation of observations from different data collection techniques, and provides an assessment of their ability to capture fault displacements features, and summarizes recommendations for future postearthquake data collection.

## THE RIDGECREST EARTHQUAKE SEQUENCE

The 2019 Ridgecrest earthquake sequence is characterized by a series of events located in a region east of the city of Ridgecrest and west of the towns of Trona and Argus in the Searles Valley ([GEER, 2019](#)). Two events produced surface ruptures on 4 and 5 July 2019, with magnitudes of M 6.5 and 7.1, respectively (the magnitudes from [Ahdi et al., 2020](#) are used). The M 7.1 event has since been identified as the mainshock, with all prior events categorized as foreshocks and subsequent events categorized as aftershocks ([DuRoss et al., 2020](#)). Tectonically, the Ridgecrest area is located within the eastern California shear zone (ECSZ), a seismically active region that accommodates about 25% of the relative displacement between the North America and Pacific plates ([Sauber et al., 1994](#)). The two main events are associated with two newly differentiated fault zones: the Salt Wells Valley fault zone for the M 6.5 event, and the Paxton Ranch fault zone for the M 7.1 event ([DuRoss et al., 2020](#)). The ECSZ is known notably for the 1992 M 7.2 Landers earthquake ([Hauksson et al., 1993](#)), the ~M 7.5 1872 Owens Valley earthquake ([Mulholland, 1894](#); [Beanland and Clark, 1994](#)), and for a five-week period of heightened seismic activity in 1995.

## STUDY AREAS AND DATA COLLECTION CAMPAIGNS

The 2019 Ridgecrest earthquake sequence triggered a significant engineering and science reconnaissance campaign involving several teams, deployed at different times following the M 6.5 and 7.1 events. Figure 1 shows the study areas and

the specific location of data collection by the different teams involved in this research. Table 1 summarizes the teams and their data collection periods and techniques. The data collection is further detailed in the subsequent sections.

The GEER team was the first on the ground ([GEER, 2019](#); [Brandenberg et al., 2020](#)). The team arrived in Ridgecrest in the late afternoon of 5 July and performed an initial survey of the M 6.5 rupture trace and of the towns of Argus and Trona to plan the following days' activities. Several photographs were taken at that time. The M 7.1 event occurred as the team was preparing to meet for dinner. The M 7.1 rupture trace was visited on 6 and 7 July, and the M 6.5 rupture trace and the towns of Argus and Trona were revisited to collect a more systematic data set. Several subgroups were dispatched to different locations to collect perishable data. The Southern California Earthquake Center (SCEC) team revisited the study areas on 11 and 12 July to refine some of the initial field data.

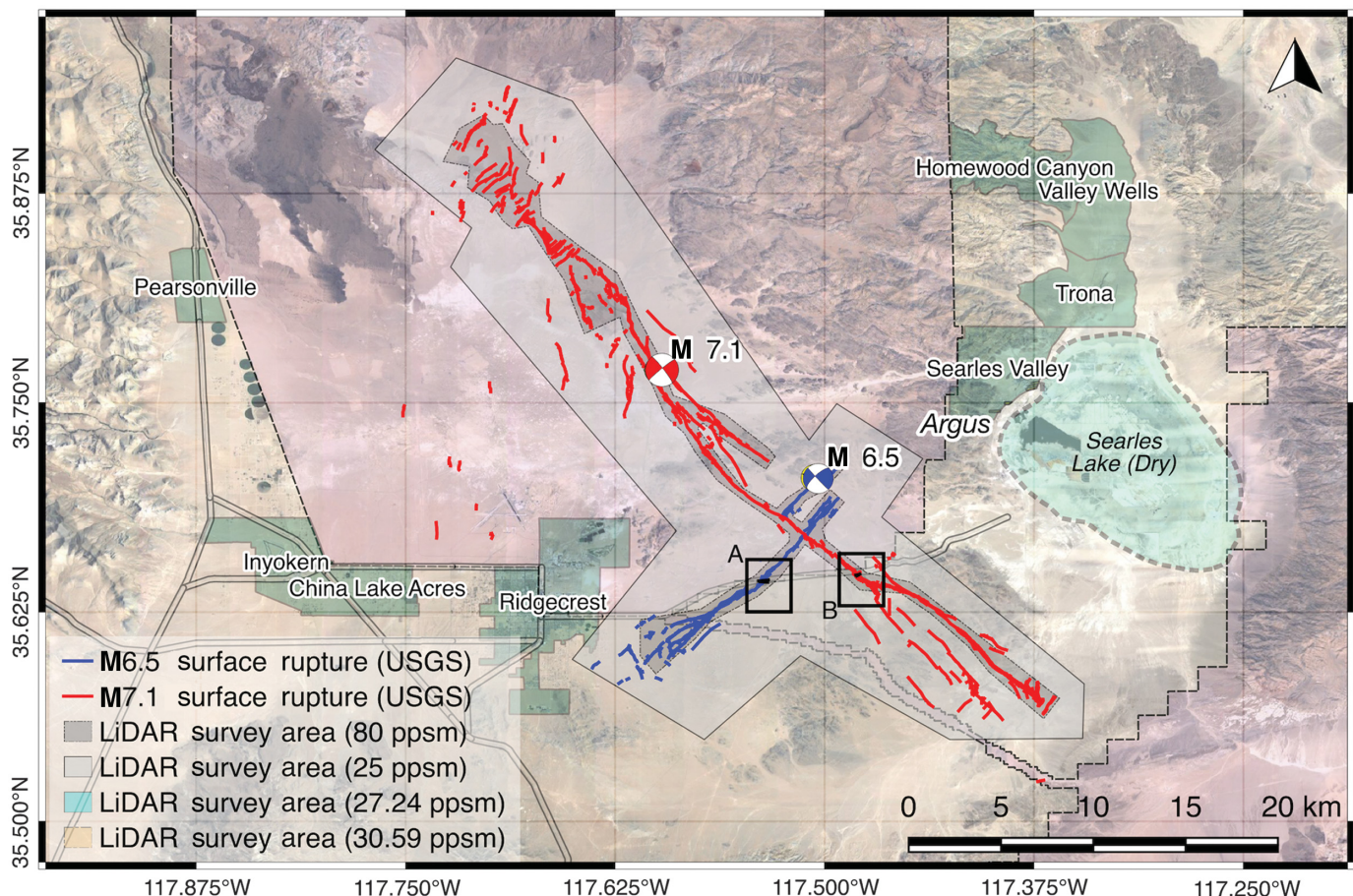
The research reported herein focused on two study areas defined for the M 6.5 and the M 7.1 fault traces, respectively (designated as A and B in Fig. 1, with larger-scale views shown in Fig. 2), and further focused on data collected along four transects. The two study areas are bounded by Highway 178 to the north and extend about 400 m to the south. The study areas were selected because of their accessibility for in-person documentation by the GEER team. The area studied represents a small area relative to the whole rupture length; however, it is wider than other field studies of off-fault microfractures (e.g., [Vermilye and Scholz, 1998](#); [Johri et al., 2014](#)), which limited their observations closer to the fault. The intent here was to compare the data collection and interpretation techniques over an area that was tractable by a single team in a day.

Three separate teams collected sUAS data in the study areas. The Jet Propulsion Laboratory (JPL in Table 1) performed their first surveys at the M 6.5 and 7.1 study areas on 9 and 11 July and completed six repeat surveys by the end of September ([Donnellan et al., 2020](#)). The GEER phase II University of Washington (UW in following instances) team performed their sUAS surveys on 16–18 July, and the GEER phase III University of California, Los Angeles (UCLA in following instances) team performed a survey of the M 7.1 study area on 10 July. The UW and UCLA teams surveyed each area once; note, their overall campaigns extended beyond the limits of the study areas described herein. Finally, lidar surveys were completed on 27 July to 2 August as part of a large National Science Foundation (NSF) Rapid Response Research (RAPID) collaborative program ([Hudnut et al., 2020](#)). Spatial coverage areas of the various aerial surveys are shown in Figure 2.

## DATA COLLECTION

### Field data collection

The field data collection was conducted on 5–7 and 10–12 July. Several approaches were used to document the surface expression of the fault traces, including following by foot the main



and secondary fault strands continuously along their full extents with waypoint geolocation, capturing geocoded photographs, and taking localized field measurements (GEER, 2019; Brandenberg *et al.*, 2020). The GEER team first coordinated with the JPL team to define study areas that they could easily survey with sUASs in a single day, targeting the rupture and off-fault cracking. This was an important constraint that supported JPL's goal to document the evolution of the fault areas over time with a unique set of control points in each of the two locations. For the purpose of this article, two transects per study area were selected: A1 and A2 for the M 6.5 trace (area A in Fig. 2); and B4 and B5 for the M 7.1 trace (area B in Fig. 2). The field transects were selected to be contained within those JPL coverage areas while spanning different expressions of the fault trace based on their visual appearance from prescreening on-foot surveys.

Each transect was surveyed by two-person teams that selected transect locations oriented perpendicular to the fault and by establishing their extents so as to completely capture visible cracks and deformations on either side of the fault. A 100 ft (30.5 m) measuring tape was laid along the transect in a relatively straight line (Fig. 3a). Overlapping photographs of the ground surface were taken at approximately 1 m (two-step) intervals along the tape (Fig. 3b,c) so as to capture a minimally disturbed continuous record of surface features. Advancing

**Figure 1.** Map showing the main traces from the M 6.5 and 7.1 events and the two study areas for this article labeled as A and B (see Fig. 2). Fault traces identified by ground and image analysis are shown in blue for the M 6.5 rupture and red for the M 7.1 rupture (Ponti *et al.*, 2020), and the light detection and ranging (lidar) survey areas of Hudnut *et al.* (2020) are indicated, with 80 and 25 points per square meter (pps m) within the dark and light gray polygons, respectively.

along the transect, the tape was sequentially repositioned as needed. Additional photographs were taken along the transect, using a 6 ft (2 m) surveyor stick for scale (Fig. 3d). Transects A1, A2, and B4 were defined following this approach. Transect B5 captured the largest deformations only and did not extend as far laterally as the other transects.

Geolocated photographs were captured with cell phones and with native apps and the “Solocator” app. Solocator saves a copy of the photograph and adds the geolocation and orientation directly on it as an overlay (Fig. 3b,c). Redundancy was provided using the “GPS Tracks” app application as a backup to the native cellphone geolocation capabilities.

#### sUAS surveys

The M 6.5 rupture was primarily mapped by UW, with JPL overlapping in the northeast corner. The area was surveyed

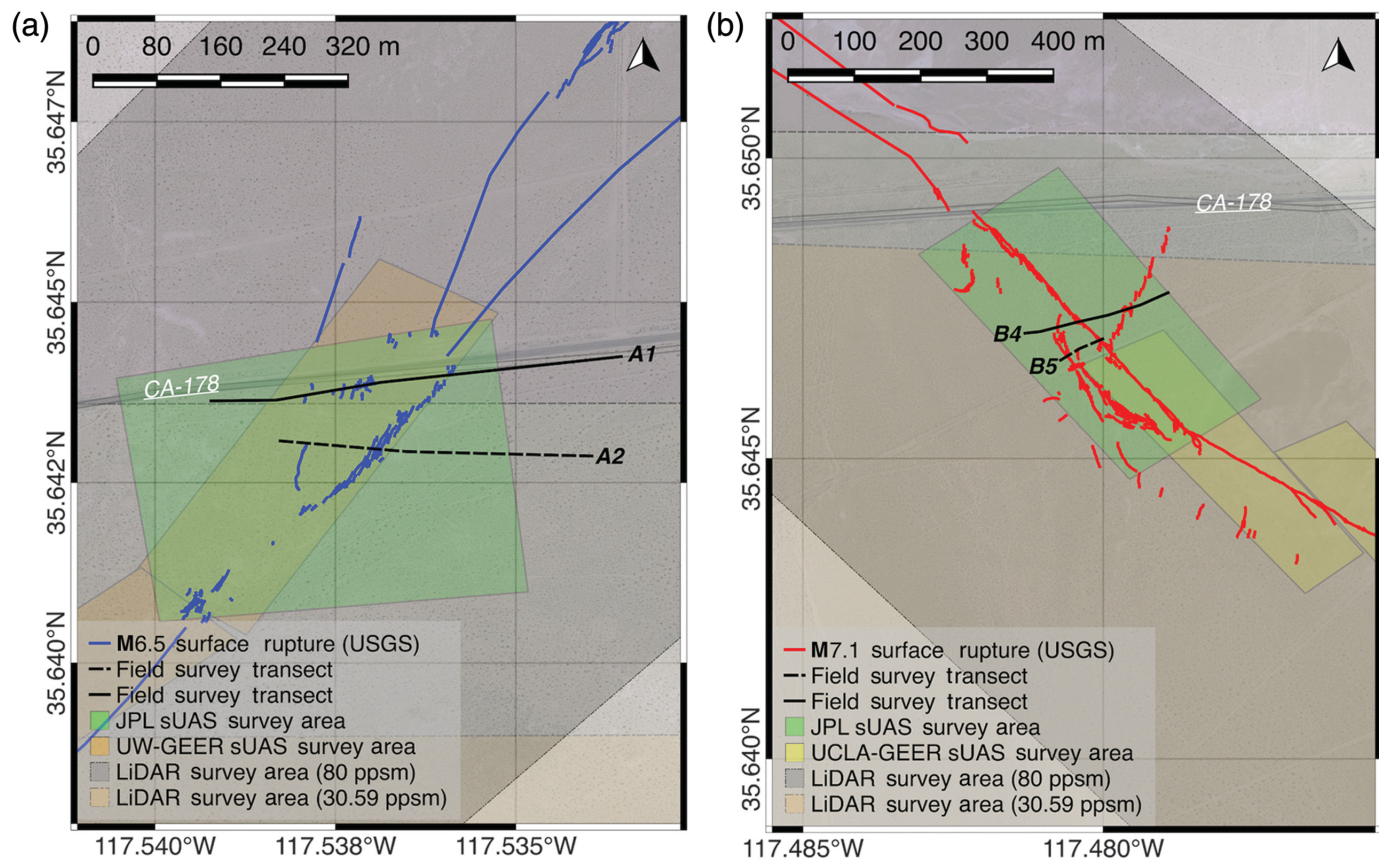


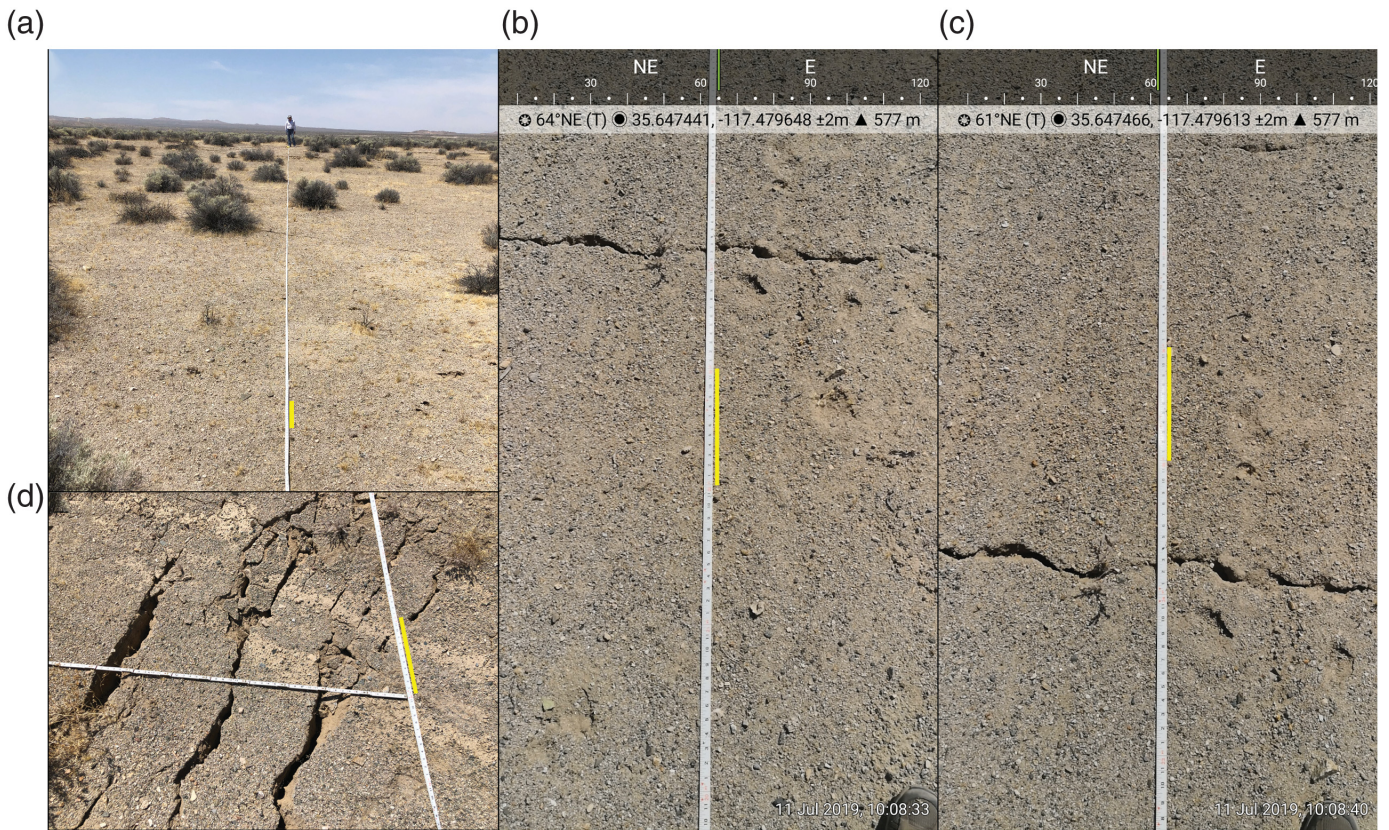
**Figure 2.** Details of (a) M 6.5 and (b) M 7.1 study areas. Each study area includes two transects along with small uninhabited aerial systems (sUAS)

and lidar surveys' extents. See Figure 1 for location.

TABLE 1  
**Summary of Data Collection Campaigns Conducted for Fault Displacement**

| Team                      | Dates (2019)                               | Data Collection Technique                                 | Team Members  | DOI   |
|---------------------------|--|---|---|---|
| GEER phase I              | 5–7 July                                   | On-the-ground photographic documentation and measurements | S. J. Brandenberg, C. A. Goulet, P. Wang, C. C. Nweke, C. A. Davis, M. B. Hudson, K. S. Hudson, S. K. Ahdi, and J. P. Stewart   | <a href="https://doi.org/10.17603/ds2-vpmv-5b34">https://doi.org/10.17603/ds2-vpmv-5b34</a> |
| NASA/JPL-Caltech          | 9, 11, 15, 22 July; 8 August; 27 September | sUAS surveys ( <a href="#">Donnellan et al., 2020</a> )   | A. Donnellan, G. Lyzenga, W. Jun, M. Pierce, and C. A. Goulet   | <a href="https://doi.org/10.5967/5sq2-rs60">https://doi.org/10.5967/5sq2-rs60</a>           |
| GEER phase II/ UW RAPID   | 16–18 July                                 | sUAS surveys  | A. Lyda, J. S. Yeung, T. Buckreis, O. Issa, S. J. Brandenberg, and Z. Yi  | <a href="https://doi.org/10.17603/DS2-TYCA-SE83">https://doi.org/10.17603/DS2-TYCA-SE83</a> |
| GEER phase III/ UCLA      | 10 July                                    | sUAS surveys  | M. A. Winters, M.-P. C. Delisle, J. T. D. Lucey, Y. Kim, Z. Liu, K. S. Hudson, S. J. Brandenberg, and T. W. Gallien   | <a href="https://doi.org/10.17603/ds2-wfgc-a575">https://doi.org/10.17603/ds2-wfgc-a575</a> |
| GEER phase IV/ SCEC RAPID | 11–12 July                                 | On-the-ground photographic documentation                  | C. A. Goulet and X. Meng  | <a href="https://doi.org/10.17603/ds2-c5z3-wy42">https://doi.org/10.17603/ds2-c5z3-wy42</a> |
| USGS and SCEC RAPID       | 27 July—2 August                           | Airborne lidar ( <a href="#">Hudnut et al., 2020</a> )    | K. W. Hudnut, B. Brooks, K. Scherer, J. L. Hernandez, T. E. Dawson, M. E. Oskin, R. Arrowsmith, C. A. Goulet, K. Blake, M. L. Boggs, S. Bork, C. L. Glennie, J. C. Fernandez-Diaz, A. Singhania, D. Hauser, and S. Sorhus | <a href="https://doi.org/10.5069/G9W094Z2">https://doi.org/10.5069/G9W094Z2</a>             |

GEER, Geotechnical Extreme Events Reconnaissance; JPL, Jet Propulsion Laboratory; NASA, National Aeronautics and Space Administration; RAPID, Rapid Response Research; SCEC, Southern California Earthquake Center; USGS, U.S. Geological Survey.



with a DJI Matrice 210 operated by UW RAPID pilots; JPL used a Parrot Anafi vehicle with an integrated 21 megapixel camera covering a  $400 \times 485$  m area. For the M 7.1 rupture trace, JPL mapped a  $460 \times 640$  m area including and adjacent to Highway 178. Finally, UCLA flew three polygons ( $\sim 500 \times 150$  m) south of the JPL area using a DJI Phantom 4 Pro with an integrated 20 megapixel camera.

JPL flew double grids (two sets of perpendicular flight paths) using pix4dcapture over each rupture at 45 m above ground level with the camera pointed  $70^\circ$  from horizontal with 80% front and 70% side overlap of the images. Fourteen iron cross ground control points (GCPs) were scattered throughout the M 6.5 survey area, and 12 GCPs were used in the M 7.1 survey area. The GCPs were surveyed using a Septentrio Real Time Kinematic system that included a base station, which transmitted corrections to the rover that was used to survey the GCPs. The position of the base station was processed using the National Geodetic Survey Online Positioning User Service Global Navigation Satellite System (GNSS) and used to correct the positions of the GCPs. Checkpoints and quality report output from Pix4D were used to estimate  $\leq 2$  cm accuracy for the GCPs intrasurvey. Accuracy between surveys due to motion of targets and survey precision is  $\leq 5$  cm (Donnellan *et al.*, 2020). The UW GCPs were measured by a Leica GS18 in base rover setup. The UCLA team used the DJI GS Pro iOS application to manage autonomous flight paths, constrained by user-defined survey extents with an image overlap of 80% (Haala *et al.*, 2013). Flight altitude was set to 55 m above ground level, providing a coverage of

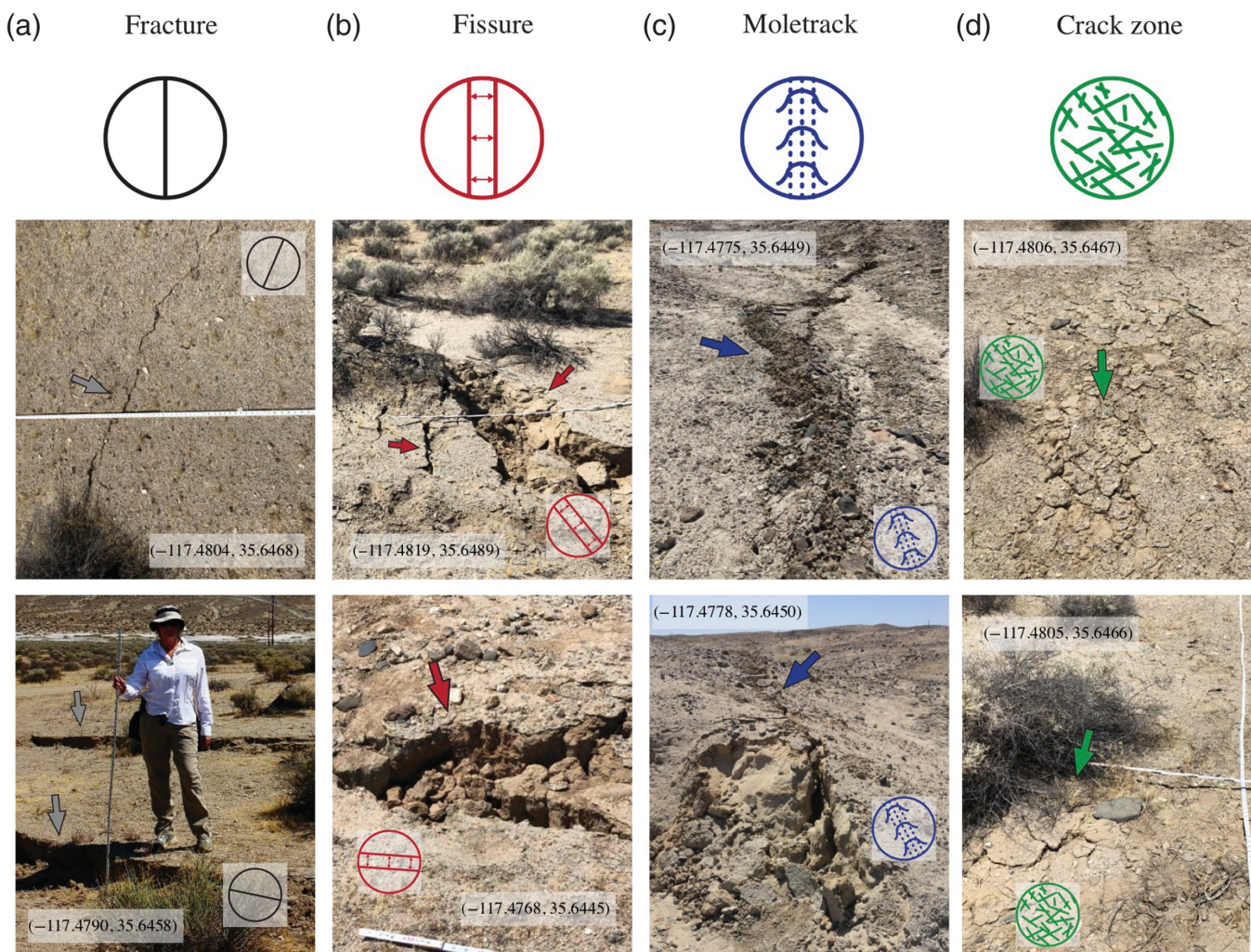
**Figure 3.** Sample pictures taken during the field data collection. (a) Measuring tape extended. (b,c) Consecutive pictures taken along transect B5 showing the overlap and the Solocator information overlay. (d) Survey stick along the tape across a complex deformation area in the M 7.1 study area. Solid yellow lines represent 1-ft-long (30.48 cm) segments along the tape for context.

approximately 6 ha (14.8 acres). The UCLA GCPs were geolocated with a Stonex S900A GNSS receiver spanning the survey region; the GCPs were constructed of  $0.3 \text{ m} \times 0.3 \text{ m} \times 1.3 \text{ cm}$  (11.8, 11.8, and 1/2 inch, respectively) plywood with a high contrast (black and white) pattern.

All sUAS collected data were processed using SfM software Pix4D or with Potree Converter in DesignSafe (Rathje *et al.*, 2017). Orthoimages, digital elevation models, and point clouds were produced and archived for each of the surveys (Brandenberg *et al.*, 2020; Donnellan *et al.*, 2020).

### Lidar imagery

On 27 July to 2 August 2019, the surface faulting and nearby surrounding areas adjacent to both the M 6.5 and 7.1 ruptures were imaged using an airborne multispectral lidar and an aerial digital camera system by the National Center for Airborne Laser Mapping. Components of this airborne geodata acquisition system and their performance characteristics are described by Fernandez-Diaz *et al.* (2016). The airborne imagery data set is georeferenced to within 5–15 cm vertical,



and 1/5500x altitude (1-sigma) accuracies, through processing of continuously operating GNSS ground-based station data, along with GNSS and gyro data from instruments mounted within the fixed-wing aircraft. Information pertaining to the Ridgecrest earthquake sequence airborne imagery data set is described by [Hudnut et al. \(2020\)](#). Imagery data are openly available (see [Data and Resources](#)). The ground sample distance of the orthoimagery product is in the 5–10 cm range.

This article used a preliminarily processed portion of the lidar data set along the M 7.1 main strand rupture for the area containing a prominent east-side-up, northwest–southeast-oriented fault scarp, located about 300–500 m southeast of Highway 178. The lidar survey area is shown in Figure 2.

## INTERPRETATION APPROACHES FOR COSEISMIC DEFORMATION DATA SETS

This section first describes a classification method for coseismic ground deformations developed to support the interpretation of field photographs. Next, the interpretation approaches used for the field photographs, the sUAS data sets, and the lidar survey data sets are summarized, with a focus on interpreting the photographs and images, supplemented by discrete field

**Figure 4.** Depiction of four main types of ground failure mechanisms resulting from surface fault rupture. (a) Fracture, (b) fissure, (c) moletrack, and (d) crack zone are represented by the labels (top row) in the supplement data product and exemplified by two photographs (bottom two rows). Arrows with representative colors highlight the distinct surface ruptures.

measurements. The interpretation of information contained in image products implies uncertainties due to (1) the complexity of the observed features and (2) the judgement of the scientist making the interpretation. Although these uncertainties are freely acknowledged, a systematic way to quantify them has not been developed as of this writing.

### Nomenclature of surface displacement features

In general, an earthquake that ruptures the ground surface results in very complex ground displacement and deformation patterns. To characterize those ground disturbances, a nomenclature based on the visual appearance and mechanics of the fault motion was defined. Using pictures obtained from the GEER and SCEC teams, the observations were classified into four major groups: fracture ([Gilbert, 2010](#)), fissure, moletrack ([Davison, 1901](#)),

and crack zone (Fig. 4). The top row in Figure 4 shows the schematic icon associated with each type of discontinuity, which can be placed and oriented in maps (such as those provided in the supplemental material), as shown in the example photographs of Figure 4. Although the term fracture is widely used in geology to define a discontinuity in structure without known origin or type of motion (Peacock *et al.*, 2016), this term is used herein to describe linear or sublinear discontinuities of ground failures that are dominantly shaped by shear rupture. Figure 4a shows examples of horizontal shear (top picture) and vertical shear (bottom picture). A fracture may occur on a nonvertical plane, and the displacement along the plane may be oblique. The database includes both fractures with and without measurable offsets (in that sense, a continuous hairline fracture is still documented but associated with a displacement of zero).

Second, surface fractures were identified with discernable extensional displacements or openings as fissures; see the two examples shown in Figure 4b.

The third type of coseismic ground failure feature is the moletrack, a term that describes a linear mounded zone of disrupted materials without a clean preferential plane of discontinuity. Moletracks are usually located along a main strand of the fault and disrupt the surface materials over variable widths. In the examples shown in Figure 4c, the surface geology is composed of sand and gravel intermixed with cobbles, providing a distinct texture to the moletrack.

The last type of ground failure feature is termed crack zone, which is used to describe an area with irregular fractures lacking consistent orientations, as shown in Figure 4d. These tend to happen in areas with a thin, brittle soil crust.

### Desktop interpretation of field photographs

Starting from the geolocated photographs taken along the transects, the discontinuities following the four categories described earlier were categorized. The classification task is not trivial as the surface expression of faulting often combines several of the idealized categories. For example, the widest feature seen in Figure 4b was classified as a fissure, but the complex surface rupture also exhibits attributes associated with fractures and moletracks. Therefore, first-order characteristics of the four classification categories were used in processing and identifying features in the field images. For each of the features, the offset and openings were estimated using the tape measure as a reference. The approximate orientation of the fracture, fissure, and moletrack features were also documented.

This information is catalogued in text files (Table S1, available in the supplemental material to this article) and Keyhole Markup Language (KML) map products (supplemental material), with the icons aligned with the strike of the feature. In cases for which multiple features were identified in a single photograph, each is catalogued separately. The ground deformations were catalogued for all the field photographs on and off the transects and are available in text and KML files in the supplemental material.

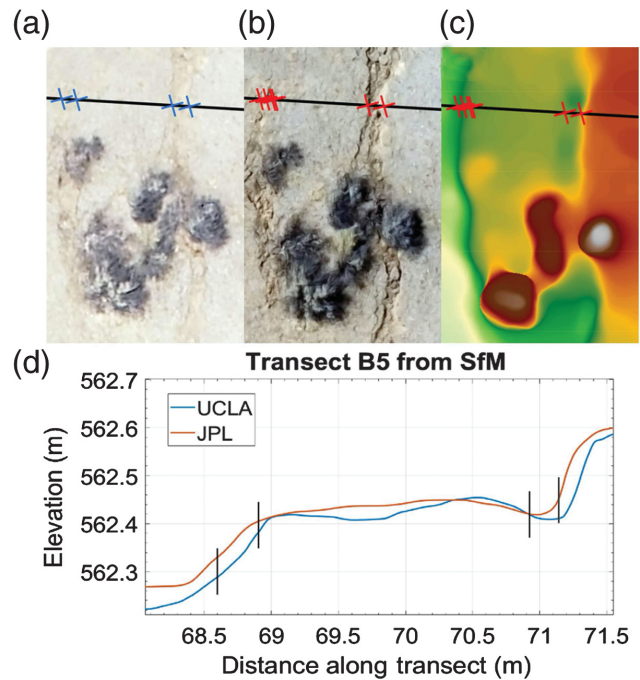


**Figure 5.** (a) University of California, Los Angeles (UCLA) orthoimage, (b) Jet Propulsion Laboratory (JPL) orthoimage, (c) digital surface model (DSM) generated from JPL orthoimages, and (d) elevation data from UCLA and JPL DSMs. Crack edges are marked by Xs in (a–c) and vertical black lines for the (a) case in (d).

The field photographs are available on DesignSafe as referenced in Goulet *et al.* (2021) and reaggregated to match this article's Electronic Supplement directory structure in Goulet *et al.* (2021), also in DesignSafe. In addition, the horizontal fissure widths estimated from the photographs along the four transects were compiled and cumulative fissure widths, from west to east, were computed for comparison to airborne data interpretations.

### Interpretation of sUAS data products

Products from SfM include point clouds, digital surface models (DSMs), and orthomosaics in both GeoTIFF and KML formats. The ground sampling distance (GSD) of the targeted areas collected by JPL just south of Highway 178 is about 1.5 cm (Donnellan *et al.*, 2020). The images were viewed in Google Earth and manually searched for ground displacement features. The cracks were traced with zoomed-in images, and any trends or lineations were then observed in zoomed out images. The traced features were exported in KML format. Multiple fault strands were identified for both the M 6.5 and 7.1 ruptures.

More quantitative approaches based on DSMs and orthomosaics were also implemented in ArcGIS to identify and quantify fissure widths. GSD ranged from 1.3 to 2.1 cm for all sUAS data, suggesting any sub 2 cm feature would be unquantifiable; from a practical perspective, a minimum of twice the GSD would be required to identify features. DSMs were examined for abrupt

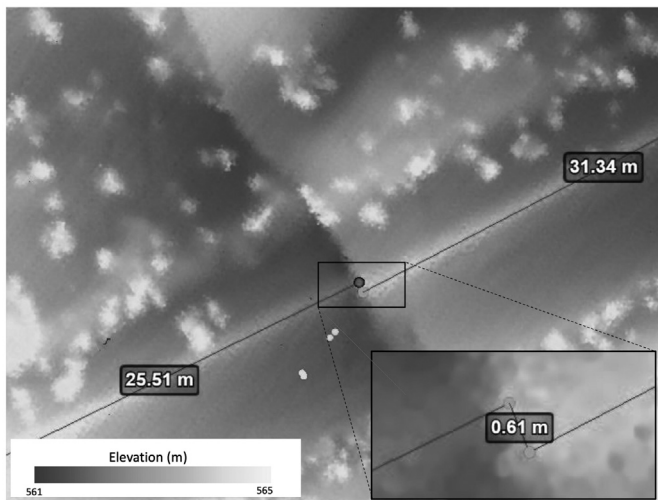


**Figure 6.** Estimation of horizontal displacement along the M 7.1 main strand using lidar data and a berm along a service road, just south of transect B5. The berm, assumed to be linear prior to being offset, is first identified on both sides of the fault trace; the measurement of the distance between the two parallel lines provides the horizontal offset (0.61 m). Shading represents elevation; blotches are vegetation and human beings.

elevation changes consistent with a rupture. In addition, the DSMs were recast using the “Slope” tool in ArcGIS to automatically identify potential displacement features. Only large fissures can be measured using the DSM or slope techniques. Smaller features were successfully identified and their width measured in orthoimagery. Edge identification may be somewhat subjective using these methods. Transects orthogonal to the fault rupture were measured at locations that were manually measured in the field. The researchers identifying and quantifying features from imagery had no knowledge of the field measurements.

The following SfM data interpretation was conducted using georectified orthoimagery analysis. Transects were visually inspected for features and marked in ArcGIS at the initial and terminating edges (Fig. 5). Fissure width was defined in the along-transect distance calculated from the marked points. An example orthoimage with two fissures is shown in Figure 5a,d. Figure 5a shows the UCLA orthoimage with (1) a 31 cm fissure from 68.59 to 68.90 m in the along-transect distance; and (2) a 36 cm fissure from 70.87 to 71.23 m in the along-transect distance. Figure 5b shows a higher resolution image of the same area from the JPL survey that reveals three distinct fissures: (1) a 13 cm fissure at 68.61 m; (2) a 5 cm fissure at 68.87 m (which ended at 68.92 m); and (3) a 34 cm fissure at 70.84 m. Essentially, the operator identified a single feature (68.59–68.90 m) in the less clear image that were resolved as two distinct cracks (68.61–68.76 m and 68.87–68.92 m) in the JPL image. The lower resolution image, from UCLA, did not specifically target transect B5, which was slightly north of the surveyed area (see Fig. 2b for the extent of the survey). Higher quality images were obtained within the targeted areas.

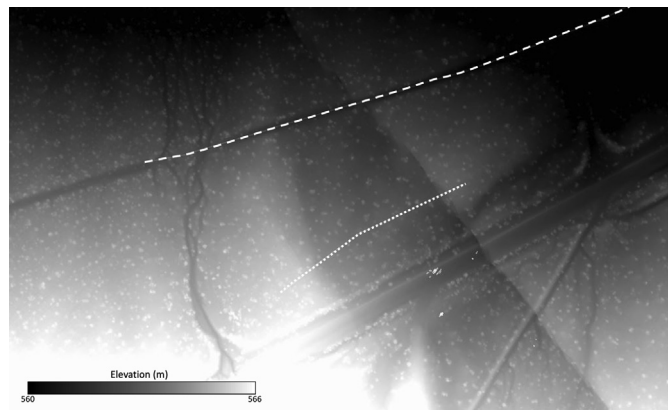
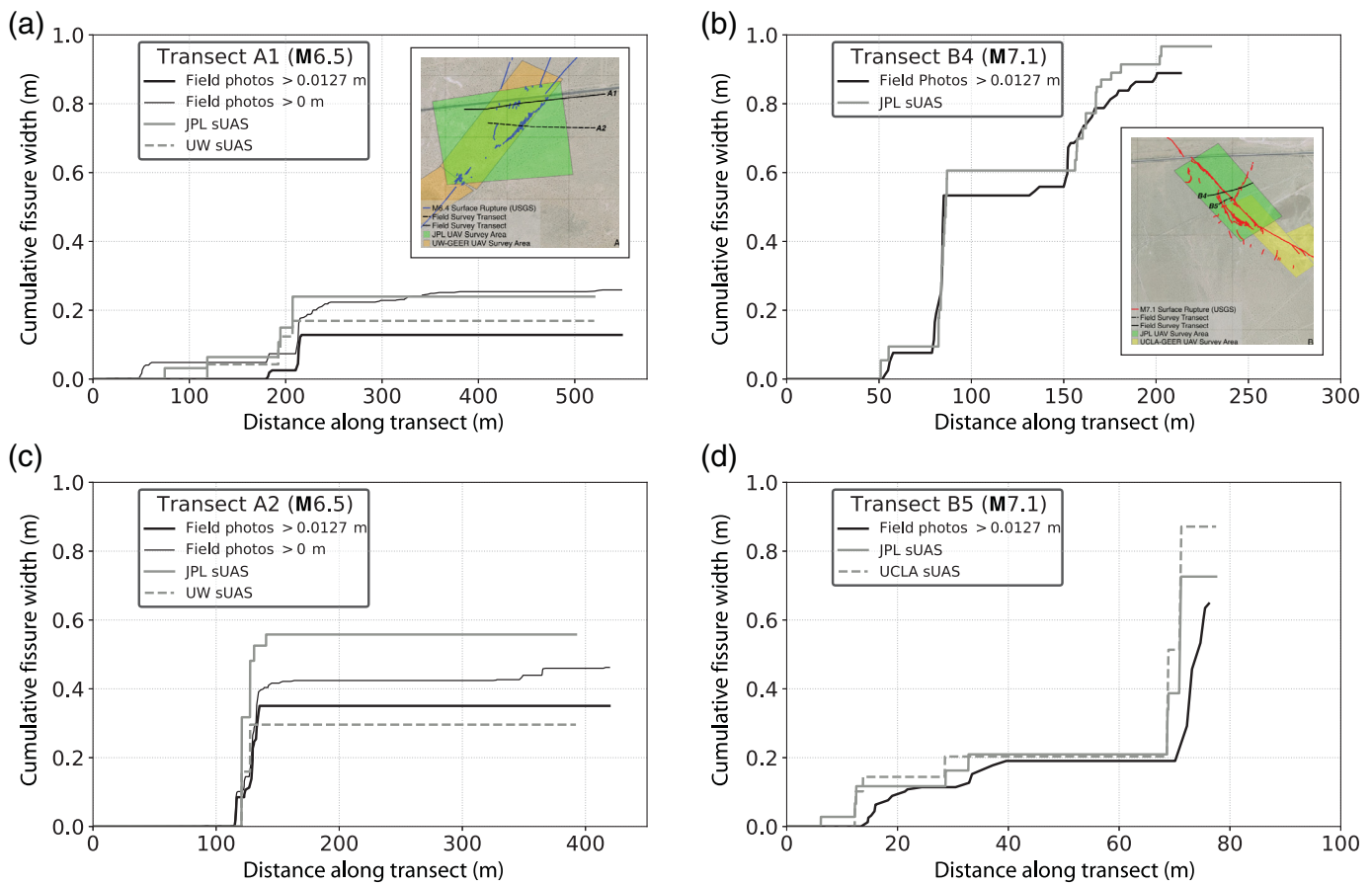


**Figure 7.** Lidar point cloud showing the southern part of the M 7.1 study area. Shading was selected to show elevation and highlight the grabenlike structure captured by transects B4 and B5 (dashed and dotted line, respectively, with B5 76 m long). Shading corresponds to elevation; blotches are vegetation and human beings.

The JPL team visited the two survey areas six times between the time of the events and the end of September 2019 (Table 1). They used the open-source software package CloudCompare to search for any postseismic deformations during the 80 days of repeated sUAS surveys. The positions of the GCPs were compared over time. Little to no deformation occurred in the two targeted sUAS areas (Donnellan *et al.*, 2020). The lack of clear postseismic deformations at either location indicates that either the two targeted sections of the M 6.5 and 7.1 earthquakes completely ruptured in the mainshock or that any possible afterslip occurred within five days of the events before the first sUAS survey took place. Continued observations will clarify whether any gradual afterslip or other postseismic motion occurred over a longer timescale over this small area of the fault rupture. Hence, the time of the different sUAS surveys is not expected to influence the ground deformation interpretations from the different teams.

### Interpretation of lidar data products

The lidar data were imported into Potree for analysis. At interpretation time, coverage was only available for the M 7.1 study area. In addition, the imagery resolution did not allow for identification of specific fissure widths along the transects. The software’s features were used to develop elevation profiles for the M 7.1 study area similar to those developed for the sUAS data sets. In addition, the permanent horizontal displacements along the main fault strand were estimated by tracking the displacement of linear features crossing the rupture (Fig. 6) for an estimate of 61 cm of horizontal displacement from lidar observations. Differencing the JPL sUAS orthoimage with pre-event Google Earth imagery shows right slip across the main M 7.1 rupture in this area of about  $70 \pm 3$  cm in the near field to up to 100 cm of slip distributed across 500 m (Donnellan *et al.*, 2020, Fig. 5).



## COMPARISON OF RESULTS

The field observations in the M 6.5 study area indicate that surface ruptures in the fault zone are broadly distributed. The pavement on Highway 178 showed several left-lateral cracks distributed over a length of about 200 m, where a section was repaved in the days following the earthquakes. In the M 7.1 study area, two main strands of the fault were identified. The strands coincided at Highway 178 but diverged to the south, creating a grabenlike structure with sunken ground between, as captured by transects B4 and B5 and visible in the lidar data (Fig. 7). Additional deformations were found over a wider area. Highway 178 was damaged as well and included some vertical offsets in addition to right-lateral displacements. Water pipes running just north of Highway 178 were damaged in both events, and gas pipelines required repairs where they crossed the M 7.1 rupture, just south of the M 7.1 study area (GEER, 2019).

In both study areas, all four types of surface damage due to faulting were observed. The most prominent features were fractures, some with vertical offsets, and fissures with variable width openings. Horizontal shear and vertical displacements were only evident near the main fault strands.

The easiest features to track from field and sUAS surveys are fissures, because it was possible to quantify the opening widths. Their study and quantification proved useful for characterizing overall deformation in the fault zone and the distribution of deformation in the strike-normal direction. A summary of

**Figure 8.** Cumulative horizontal fissure widths along the four transects for the (a,c) M 6.5 and (b,d) M 7.1 study areas.

fissure interpretations in terms of cumulative horizontal widths along each of the four transects are shown in Figure 8 from west to east. Figure 8a,c shows the results from the field along with those from the JPL and UW sUAS for the M 6.5 study area along transects A1 and A2. For this event, all the measurable fissure widths were recorded from the field photographs; the field tape measure was in feet with one eighth of an inch (0.3175 cm) as the shortest unit. Figure 8b,d shows the results for transect B4 from the field and JPL sUAS and for transect B5 from the field and sUAS data from JPL and UCLA. For this event, only fissure widths larger than half an inch (1.27 cm or 0.0127 m) were recorded. Field interpretations with this width limitation are provided for transects A1 and A2 as well to facilitate a visual comparison.

For the field photo interpretation, it was estimated that the range of uncertainty was on the order of one or two eighth(s) of an inch (0.3175–0.635 cm) for fissures one inch (2.54 cm) or larger, depending on the specifics of the images, even though measurements were made right along the tape. The contributors to this uncertainty include: (1) even at the scale of the tape, the fissure width can vary laterally; and (2) some pictures may include shadows or parallax effects if they were

TABLE 2

**Selected Cumulative Fissure Widths along Transects as Shown in Figure 8**

| <b>Method</b>         | <b>A1 (400 m)</b> | <b>A2 (200 m)</b> | <b>B4 (125 m)</b> | <b>B4 (200 m)</b> | <b>B5 (50 m)</b> | <b>B5 (76 m)</b> |
|-----------------------|-------------------|-------------------|-------------------|-------------------|------------------|------------------|
| Field $\geq$ 0 m      | 0.2540            | 0.4242            | —                 | —                 | —                | —                |
| Field $\geq$ 0.0127 m | 0.1283            | 0.3505            | 0.5334            | 0.8787            | 0.1905           | 0.6477           |
| sUAS JPL              | 0.2396            | 0.5579            | 0.6060            | 0.9144            | 0.2097           | 0.7260           |
| sUAS UW               | 0.1692            | 0.2959            | —                 | —                 | —                | —                |
| sUAS UCLA             | —                 | —                 | —                 | —                 | 0.2033           | 0.8714           |

The measurements were made in inches and are reported in m; all four digits of the conversion were retained for easy recovery. JPL, Jet Propulsion Laboratory; sUAS, small uninhabited aerial systems; UCLA, University of California, Los Angeles; UW, University of Washington.

not taken exactly in the horizontal position or if the tape was not sitting exactly on the ground. This range in measurement uncertainty for fissures wider than one inch is representative of most cases.

Interpretations from field photographs tend to capture smaller features and lead to smoother progressions of cumulative displacements along the transects compared to those from the airborne data sets (Fig. 8), especially in the case of transects A1 and A2. The resolvable resolution of the sUAS SfM products allowed identification of only the largest features, and displacements were concentrated at fewer discrete points.

Along transect A1 (Fig. 8a), five fissures ranging from 3.2 to 9.0 cm were identified in the JPL sUAS data products, whereas four fissures ranging from 3.7 to 4.7 cm were identified in the UW sUAS processed observations. The cumulative fissure width was 17 and 24 cm for the JPL and GEER phase II imagery, respectively. Along transect A2 (Fig. 8c), four fissures were identified in the JPL products and two in the UW products. Cumulative fissure width was 59.8 and 29.5 cm for the JPL and UW observations, respectively.

Along transect B4, JPL interpreted 28 fissures ranging from 1.5 to 8.3 cm. Notably, at 85 and 157 m (Fig. 8c) in the along-transect distance, multiple small fissures ( $\sim$ 1.5 cm) near the GSD were identified. Transect B5 was slightly north and external to the ground-controlled region of the UCLA measurements. Although this area was not specifically targeted by that team, data were available and analyzed. In the JPL observations, eight fissures ranging 2.7–33.9 cm were observed along transect B5 (Fig. 8d) compared to six visible fissures ranging from 4.1 to 35.7 cm in the UCLA observations. The largest differences were observed for the M 6.5 area (Fig. 8a,c). For both transects, there are substantial differences between the interpretation of the distinct sUAS data sets. At 400 m along transect A1 (Fig. 8a), the JPL sUAS estimate is 94% of the field estimate, compared to 67% for the UW sUAS estimate, with both sUAS maximum measurements reached at 207 m, right after the largest deformation zone (Table 2). Transect A2 shows large differences across all the data sets. Once again using a point along the transect after the largest deformations were observed (200 m), the JPL sUAS estimate is 132% that of the field with the UW sUAS estimate only 70% that of the field,

each value plateauing at 160 and 130 m, respectively (Table 2). By only considering measurements of 1/2 inch (1.27 cm) and above, which were reported for all the methods, then the sUAS estimates overpredicted the field measurements for A1; for A2, JPL's overprediction was larger and UW's underprediction was lower (Table 2). The fit among the methods is overall better for B4 and B5 (Fig. 8b,d and Table 2).

To better understand the reason for these differences, histograms of the fissure widths were produced (Fig. 9). Fissure widths from the field are shown in gray on all four panels of Figure 9. Except for the case of B4 (Fig. 9b), the sUAS estimates are all above 0.0254 m (1 inch). This is consistent with the expected 2 cm resolution accuracy described in the sUAS section (although JPL was able to estimate narrower fissures for B4). Figure 9 also shows that the field interpretations led to a larger number of smaller fissure widths than obtained from an interpretation of the sUAS. This trend is more important for transects A1 and A2, in which a broader distribution of widths was captured in the field data set (recall that for those two transects, all non-zero widths were compiled). In the case of A1 and A2, the overprediction of JPL sUAS results noted above is completely accommodated by the interpretation of a handful of wider fissures. For transect B4, the distribution among the methods is the closest of all the cases (Fig. 9b), and the overall cumulative widths are comparable (Fig. 8b). However, for B5, none of the methods show similar trends in the distribution of fissure widths (Fig. 9d), yet the cumulative width results are generally good among the methods (Fig. 8d). A fissure-width assessment that compared the results with the lidar data set was not performed. Because of its pixel-size resolution and the distribution of the fissure widths highlighted here, the outcome of this exercise was not expected to be informative.

Fault zones tend to exhibit distributed deformations that can make field measurements quite difficult. Figure 10 illustrates this with a photograph taken along transect B4 just west of the main M 7.1 fault strand, looking east (near the 77 m mark in Fig. 8b). Individual offsets across this zone are quite difficult to measure in the field. The total right-lateral horizontal offset across the zone was estimated at about  $30 \pm 3$  cm using field equipment and continuous road track offsets as reference.

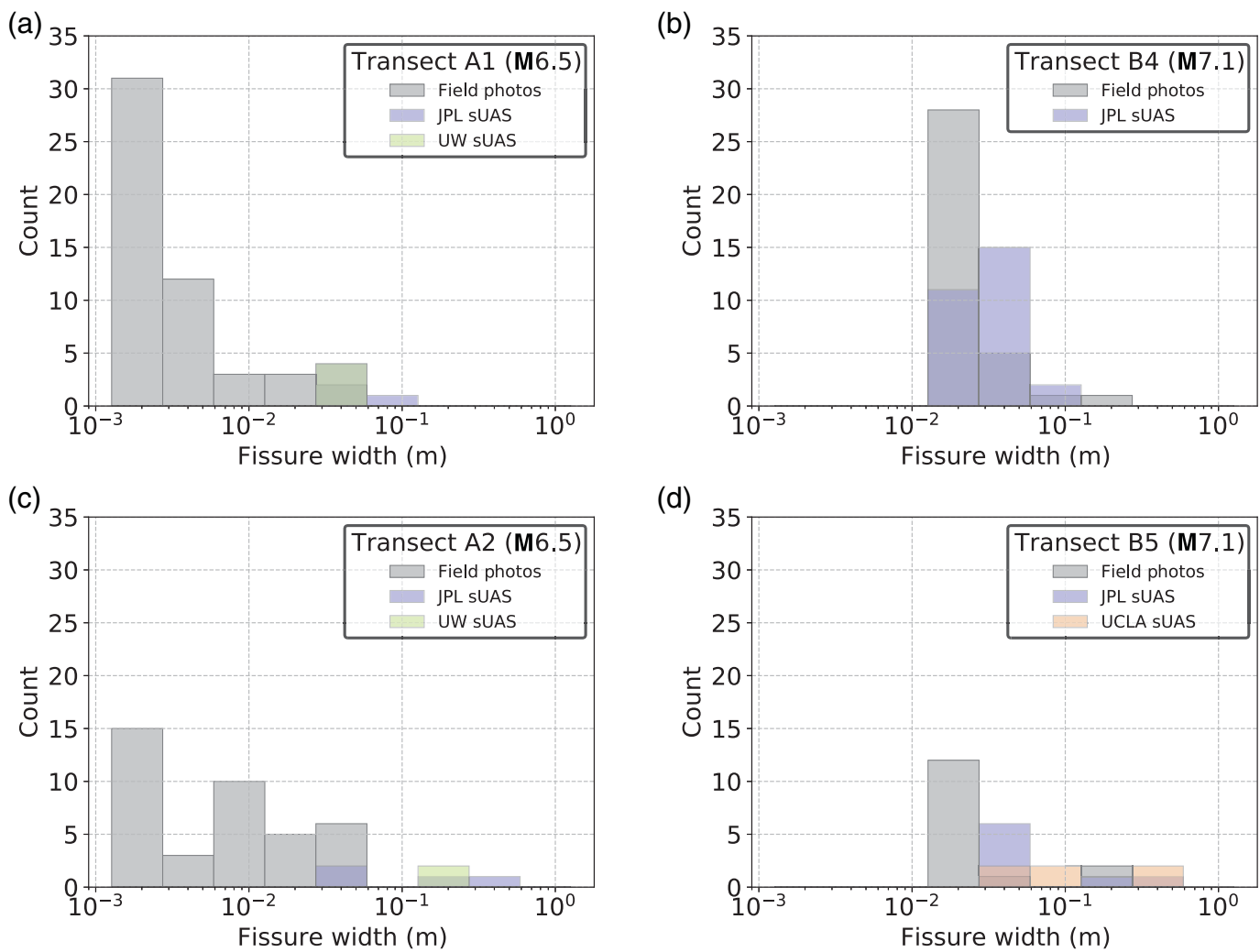
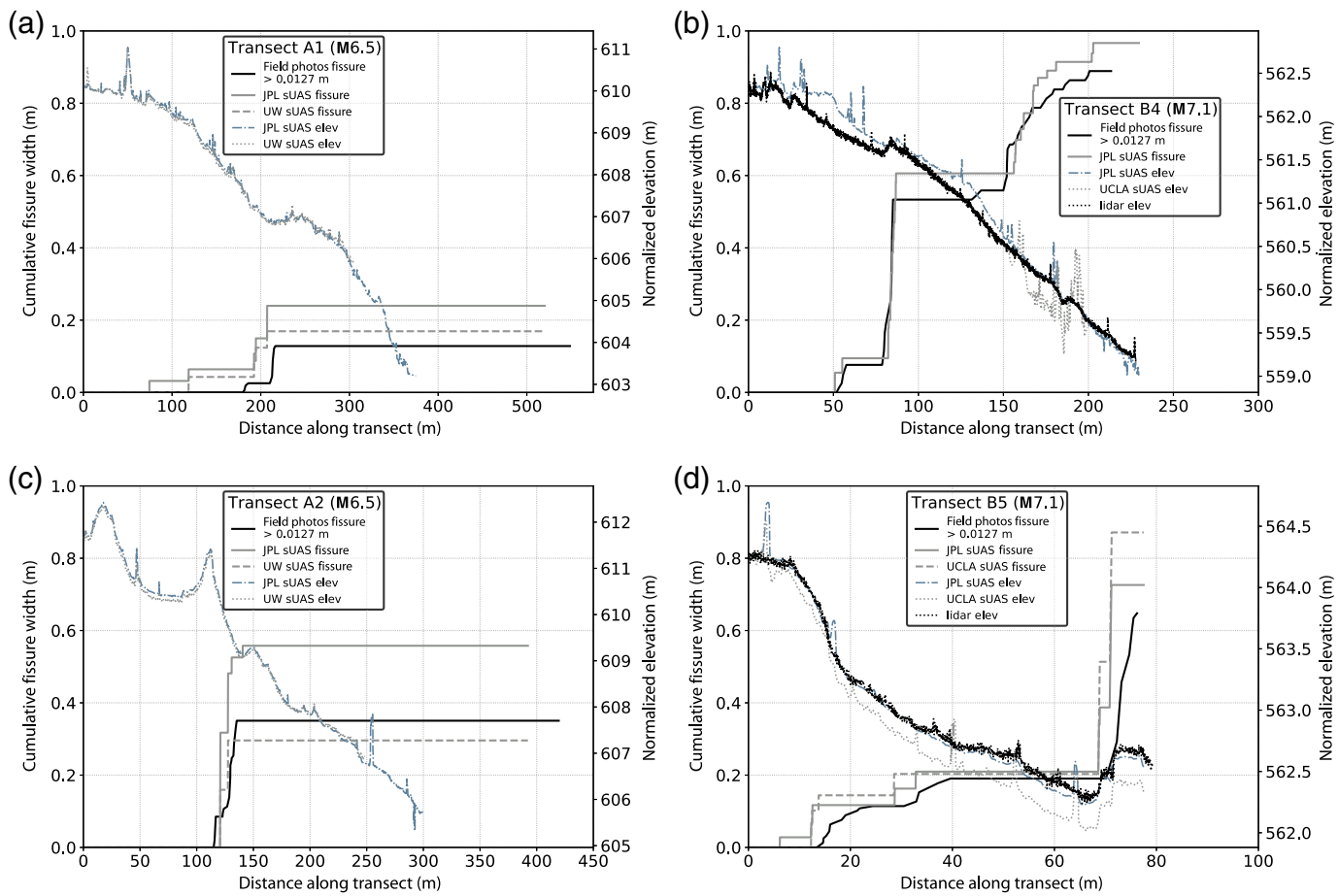


**Figure 9.** Histogram of horizontal fissure widths along the four transects for the (a,c) **M** 6.5 and (b,d) **M** 7.1 study areas.

Vertical offsets are in general more difficult to measure, especially if they are small, as was the case at this location. Using tools available in the field, the vertical offset was estimated to be on the order of 20 cm for the zone. The assessment of vertical offsets such as these can greatly benefit from sUAS and lidar surveys. Figure 11 shows elevation cross sections obtained from the sUAS data sets along the four transects and overlaid on the cumulative displacement data. The upward spikes in the elevation plots are due to the presence of vegetation and could be removed from the data (a processing step not applied herein). However, the remaining changes in elevation correlate very well with the largest displacement zones. For the location shown in Figure 10, the elevation survey from the JPL imagery shows a vertical offset of 20 cm in the 77–82 m distance range along transect B4 (Fig. 11b and data in the supplemental material). On its own, this elevation difference could not be interpreted as a fault displacement; however, it was identified as such after an examination of additional data from orthomosaics and field observations. Similarly, vertical offsets have been measured in the 66–72 m range at the eastern edge of transect B5 (Fig. 11d and data in the supplemental material). This zone exhibited staircase-like vertical



**Figure 10.** Complexity of **M** 7.1 main strand rupture along transect B4 looking east. The heavily damaged zone is approximately 5 m wide at this location.



displacements that were easier to measure than those shown in Figure 10. Field measurements at that location indicated a cumulative vertical offset of  $40 \pm 3$  cm, whereas the JPL elevation data measured a 40 cm offset (Fig. 11b). The lidar only covered the M 7.1 area, and the elevations captured around the B5 track those from JPL sUAS very well but are close to the UCLA sUAS results for B4.

## DISCUSSION AND LESSONS LEARNED

Although the specific values of displacement can differ, the aerial and field approaches seem equally adept at capturing the main zones of deformation. While it does not come as a surprise that fissures with widths below the accuracy of the sUAS method were not captured, what is striking is that when a fissure was detected by sUAS, it tended to be larger than its field observation. Given the data set, which consists mostly of relatively fine fissures, it is hypothesized that this is due to three main causes:

1. The pixels within a fissure are very dark relative to the surrounding ground and if pixels straddle a fissure (which is arguably the most likely case as pixels cannot systematically be all aligned and contained within fissures), their color will be smeared, leading to under or overassessment of the width. However, because the field surveys and photographs

**Figure 11.** Elevation along transects obtained from sUAS data sets superposed on Figure 8 along the four transects for the (a, c) M 6.5 and (b, d) M 7.1 study areas. The UCLA and UW elevations were repositioned based on the JPL data absolute elevations. The color version of this figure is available only in the electronic edition.

tended to reveal narrower fissures than the 2 cm sUAS accuracy, there were not as many underpredictions as there were overpredictions.

2. Shadows may occur if there is vertical displacement or if the soil near the fissure edges is disturbed, with both phenomena leading to darker shades over a broader zone in the sUAS images. In the first case of shadows, the overprediction will depend on the time (i.e., the position of the sun relative to the fissure-crack combination) and the dip of the fault. In the case of damage near the fissure edges, the interpretation may lead to capturing the outer edge of the fissure, compared to the inner edge from a field observation where the shade is clearly seen as damage. This effect can be compounded if there are a lot of fissures within a small area. Figure 10 shows an example of that situation. The broad deformation zone along B4 that could be observed as a series of small fissures from the field was interpreted as fewer wider fissures from the sUAS imagery.

3. Because the transects were defined as lines, there is a possibility that the aerial interpretations did not exactly follow the field lines, even with careful geolocation across the methods. Although great care was taken to align the sUAS surveys with the field surveys, using geolocated overlays, and pictures, the lidar results were not as carefully aligned. The near-perfect alignment of elevation estimates along A1 and A2 (Fig. 11a,c) infer that the JPL and UW sUAS surveys captured the same line; however, differences between the sUAS and lidar results hint that the methods might have sampled different lines. This could be remediated by placing field markers at the transect ends to be captured by the aerial methods or by defining the transects to have a nonzero finite width picked to span the potential geolocation drift across methods.

Performing a calibration exercise with a data set that includes a larger number of fissures wider than the accuracy threshold could provide more insight on items 1 and 2. However, if individual surficial fissures less than about 2 cm are not of critical importance for a design project or for PFDHA in general, the differences cataloged here are likely not significant. An argument to the contrary could be made in the case of transect A2, but that would have to be considered in the context of the uncertainties captured by the PFDHA model itself.

An initial assumption was that field measurements would serve as the ground truth against which to test the data sets from sUAS and lidar. This exercise demonstrated that aerial techniques present unique advantages over the field methods, and that no one data set should be taken as the ground truth. All data sets should be considered based on their reliability to capture specific metrics. Field documentation as reported herein is best at capturing high-resolution horizontal deformations. It is very difficult to measure vertical offsets over wide deformation zones (up to several meters) in the field, and this is something for which the aerial methods are better suited. Fieldwork is necessary to collect precise information and images as well as to develop an understanding of the complexity of fault ruptures. Yet, a combination of techniques including methods such as SfM from sUAS, in addition to on-the-ground field observations, has the potential to offer more useful data products to the science and engineering communities interested in quantifying displacements due to fault rupture. Overall, the advent of improved aerial systems, such as sUAS, allows for data collection that is systematic, continuous over a large area, and fast, compared to on-the-ground surveys. The development of powerful SfM software makes processing transparent and reproducible, and, more important, enables multiple teams to highlight different data characteristics. This is also an advantage, relative to on-the-ground fieldwork, that depends on human perception under potentially difficult field conditions, such as heat in this case.

The SfM results from the sUAS surveys proved extremely useful for identifying ground displacement features and fault

splays. Data products were analyzed in the office by scanning the full extent of surveys manually and using automated techniques. The results showed the complexity of the surface deformation with lineations that were as narrow as a single fracture or en echelon fissures forming zones up to 15 m wide. Subparallel and conjugate fault splays were also identified in the imagery. GCPs improved the solutions, which constrained the geometry of the final product, thus making it possible to compare repeated surveys.

Lidar data are valuable for the study of large areas at relatively high resolutions. They allow the systematic capture of lateral and vertical displacements due to fault rupture in a fashion similar to sUAS, but over a much larger area. Given the limited scope of this research, the lidar data showed good agreement with other techniques. Lidar is expensive and requires extensive logistical planning, which makes it a less accessible technique.

The benefit of field photographs providing high-resolution images was clear, as shown by the smooth lines in Figures 8 and 10. In field surveys, teams should consider taking pictures of the same feature from several angles so as to process them with SfM software in the office as a supplement to aerial imagery. An alternative approach could be to have the sUAS fly at a much lower altitude over limited areas. This may require adapting the GCP systems to shorter distances.

This work was motivated by practical engineering concerns related to on-fault and off-fault deformations that can affect distributed infrastructure. Lessons learned for future post-earthquake reconnaissance studies about these specific objectives include:

- The field team originally relied on documenting ground deformation features with photographs and then estimating the displacements in an office environment. Although this worked reasonably well for fissures, it was more difficult for shear fractures, especially for those with vertical offsets. Broad deformation zones (moletracks and cracked zones) are equally difficult to characterize in the field and from photographs.
- Geotagging of the camera images is critical to postfield data interpretation. Ideally, the metadata should include the location (latitude and longitude) and the orientation of the camera.
- Because of overheating of the equipment, team members sometimes alternated in taking pictures while one device was cooling and/or charging. This caused a mismatch in the geotagging locations coming from different devices, which was addressed using the continuous tape as the location ground truth. Unfortunately, this required substantial work to compare Global Positioning System (GPS) locations, time stamps, and tape-measure locations. For the second field trip, ice packs and powerful USB chargers were carried in a belt bag or used with the sUAS vehicles and batteries; this solution substantially reduced overheating downtime and simplified the process for subsequent data alignment from multiple devices.

- The focus study areas were selected because of their accessibility. However, this accessibility also meant that the ground surface was more susceptible to damage from “earthquake tourism” and news media crews. This highlights the need for reconnaissance teams to capture easily accessible, perishable fault displacement data very quickly after the event. Nonetheless, future reconnaissance teams interested in validating displacement should select a study area that is less conspicuous to avoid the destruction of the critical features while the data collection is ongoing. This is important as it may take a few days to deploy sUAS surveys and even longer to perform lidar campaigns.
- Ideally, sUAS SfM interpretation should be completed by at least two independent teams. When discrepancies are noted, field pictures and additional visits can be used to provide a definitive assessment.

## CONCLUSION

This article highlights the importance of characterizing fault displacements for the development of PFDHA models as distributed infrastructure can be affected by localized fault displacements and strains over larger distances. For example, distributed strains represent an important factor in high-speed rail applications. Usually, postevent displacement data collection focuses effort on the areas of largest displacements, on or very near main fault strands. Current displacement databases are often populated with incomplete data sets in this regard (e.g., [Sarmiento et al., 2019](#); [Baize et al., 2020](#)), and the literature provides little insight on whether the lack of observed displacement corresponds to zero displacement or to the fact that a site was not surveyed.

Recent developments in low-cost aerial survey techniques—in addition to satellite imagery and lidar—provide the opportunity to collect perishable data over large continuous areas but have not been formally validated against field observations collected for that purpose. As part of the Ridgecrest reconnaissance work, the opportunity arose to design a validation exercise across different data collection and interpretation techniques. The study aperture was selected to capture the complete width of ruptures along discrete transects perpendicular to the fault traces and to document surface expressions of the coseismic rupture that include, but are not limited to, primary fault displacement. The study was developed in the field and the data collection was coordinated among the different teams (field, sUAS, lidar).

Key conclusions are as follows:

- There is generally good agreement between field and aerial interpretations of fault deformation from the two Ridgecrest main events. Although the details captured in the field were not necessarily captured by the sUAS surveys, the location and width of main deformation zones were consistent among methods. The differences observed are generally

small, but when developing PFDHA models, they could inform the minimum variability to be considered around observational data sets.

- The use of fissures as a proxy for deformation can lead to an overprediction from sUAS relative to field measurements, especially when the fissures are smaller than or near the pixel resolution. This is due to the interpretation of pixel colors subjected to smearing effects, especially if the edges of the fissures are damaged.
- For future event reconnaissance, if possible, extensive use of sUAS data collection is recommended. The collection of larger data sets to allow a more quantitative event-specific comparison of results across different methods is recommended as well. Focused validation sections as selected herein are ideal but would provide more value if they spanned different environments within the rupture region. In addition, the transects provided herein are defined as linear and only captured features along that line during the data interpretation of the photographs. Given the large spatial variability of damage features within short distances, a slight mismatch of that line on SfM and lidar survey maps could also lead to a mismatch in the interpretation. Hence, it would be preferable to systematically consider a band around the transects and to identify features within that band to account for potential discrepancies in geolocation from different data collection methods and devices.
- There is an advantage to forming a validation team at the beginning of the reconnaissance work to coordinate on perishable data collection strategies and validation objectives.
- In areas where field visits are not possible or access is difficult, it has been demonstrated that aerial surveys can be relied upon, provided they are in a generally similar setting as the validation area. The extrapolation of the results presented herein would not be appropriate, for example, to an urban area.
- A classification scheme of surface damage features to support numerical modeling activities has been developed. The categories were based on the features’ appearance and how they can express different inelastic behavior of the rock and surficial deposits they perturb. These observations can help scientists better understand fault maturity and related modeling concepts related to fault maturity ([Power and Tullis, 1991](#); [Sagy and Brodsky, 2009](#)), as well as to support the validation of emergent numerical models implementing structure mechanics (e.g., brittle failure) or discrete elements for fault displacement (e.g., [Benesh et al., 2007](#)). The definition of ground displacement and surface expression of faulting beyond primary on-fault slip provides a unique data set for the calibration and validation of such computer-based simulation models.

Based on this work, the use of complementary techniques is recommended to collect fault displacement data following

surface-rupturing earthquakes. Ideally, following a large event, resources should be made available for a lidar survey as well, even if those surveys can rarely be completed with short notice. There is very little use of the lidar data herein. This is due partially to the resolution of the orthoimagery relative to the dimension of the displacement features for those two events in the study areas. However, the elevation profiles showed good agreements and can be used in a continuous fashion across wide areas, which presents an advantage over sUAS surveys. The latter are generally faster to deploy, at a much lower cost, and do not require large teams (two people can be sufficient for each survey area). It is important for sUAS teams to set up GCPs to ensure that high-quality data are collected that can be accurately processed. Coordination of sUAS teams to provide complementary coverage is also important, but some overlap is recommended to ensure data continuity across different data sets.

## DATA AND RESOURCES

The data presented in this article are publicly available and have been assigned digital object identifiers (DOIs), as summarized in Table 1. Software: Solocator - Global Positioning System (GPS) Field Camera Version 2.12 (v.2.12) available at <https://solocator.com>; GPS Tracks (v.3.5.1) is available at <http://www.dmsolutions.com>; Pix4D software is available at <https://www.pix4d.com/>; Potree point cloud renderer is available at <https://potree.org>; Google Earth is available at <https://earth.google.com/>; CloudCompare software is available at <https://www.danielgm.net/cc/>. The supplemental material includes the data used to generate figures and electronic table of displacement features catalogued from field photographs and its associated Keyhole Markup Language (KML) file and the pictures referred to in the supplement have been aggregated in [Goulet et al. \(2021\)](#). Lidar imagery data are available at <https://opentopyography.org>. All websites were last accessed in July 2021.

## DECLARATION OF COMPETING INTERESTS

The authors acknowledge there are no conflicts of interest recorded.

## ACKNOWLEDGMENTS

This work was supported in part by the Southern California Earthquake Center (SCEC), SCEC Contribution Number 10966, and by the Rapid Response Research (RAPID) National Science Foundation (NSF) award (Grant Number EAR-1945781). SCEC is funded by the NSF and U.S. Geological Survey (USGS) through cooperative agreements EAR-1600087 and G17AC00047 respectively. Additional funding for this work was provided by the Pacific Gas & Electric Company (PG&E). The Geotechnical Extreme Events Reconnaissance (GEER) Association work was supported in part by the NSF through the Geotechnical Engineering Program under Grant Number CMMI-1826118. Portions of this work were carried out by the Jet Propulsion Laboratory (JPL), California Institute of Technology, under contract with National Aeronautics and Space Administration (NASA). The authors thank Andrew Lyda, J. Sean Yeung, and the University of Washington (UW) RAPID facility for their small uninhabited aerial systems (sUAS) imaging work for the M 6.5 rupture. The authors thank the

Ridgecrest Sequence California Earthquake Clearinghouse, coled by Anne Rosinski and Cindy Pridmore, with support from Heidi Tremayne, Maggie Ortiz-Millan, and others from the Earthquake Engineering Research Institute. The authors would like to thank the following individuals for their support: Niket Agrawal, Pinkal Panchal, and Gabriel Martinez (Ridgecrest Super 8). The authors would like to thank Yousef Bozorgnia, Luis Dalguer, Albert Kottke, Greg Lavrentiadis, Chris Milliner, Rob Moss, and Steve Thompson, from the Fault Displacement Hazard Initiative (FDHI), with an extra special acknowledgement to Alex Sarmiento for her continued support and helpful suggestions. Finally, the authors thank Rich Briggs, Robert Zinke, and an anonymous reviewer whose comments helped to improve the article.

## REFERENCES

- Ahdi, S. K., S. Mazzoni, T. Kishida, P. Wang, C. C. Nweke, N. M. Kuehn, V. Contreras, B. Rowshandel, J. P. Stewart, and Y. Bozorgnia (2020). Engineering characteristics of ground motions recorded in the 2019 Ridgecrest earthquake sequence, *Bull. Seismol. Soc. Am.* **110**, no. 4, 1474–1494, doi: [10.1785/0120200036](https://doi.org/10.1785/0120200036).
- Ashby, M. F., and C. G. Sammis (1990). The damage mechanics of brittle solids in compression, *Pure Appl. Geophys.* **133**, 489–521, doi: [10.1007/BF00878002](https://doi.org/10.1007/BF00878002).
- Baize, S., F. Nurminen, A. Sarmiento, T. Dawson, M. Takao, O. Scotti, T. Azuma, P. Boncio, J. Champenois, F. R. Cinti, et al. (2020). A worldwide and unified database of surface ruptures (SURE) for fault displacement hazard analyses, *Seismol. Res. Lett.* **91**, 499–520.
- Beanland, S., and M. M. Clark (1994). The Owens valley fault zone, eastern California, and surface faulting associated with the 1872 earthquake, *U.S. Geol. Surv.*, Report No. 1982, 38 pp.
- Benesh, N. P., A. Plesch, J. H. Shaw, and E. K. Frost (2007). Investigation of growth fault bend folding using discrete element modeling: Implications for signatures of active folding above blind thrust faults, *J. Geophys. Res.* **112**, no. B03S04, doi: [10.1029/2006JB004466](https://doi.org/10.1029/2006JB004466).
- Brandenberg, S. J., J. P. Stewart, P. Wang, C. C. Nweke, K. Hudson, C. A. Goulet, X. Meng, C. A. Davis, S. K. Ahdi, M. B. Hudson, et al. (2020). Ground deformation data from GEER investigations of Ridgecrest earthquake sequence, *Seismol. Res. Lett.* **91**, no. 4, 2024–2034, doi: [10.1785/0220190291](https://doi.org/10.1785/0220190291).
- Cundall, P. A., and O. D. L. Strack (1979). A discrete numerical model for granular assemblies, *Geotechnique* **29**, 47–65, doi: [10.1680/geot.1979.29.1.47](https://doi.org/10.1680/geot.1979.29.1.47).
- Davison, C. (1901). The Great Japanese earthquake of October 28, 1891, *Geogr. J.* **17**, no. 6, 635–655.
- Donnellan, A., G. Lyzenga, W. Jun, M. Pierce, and C. A. Goulet (2020). Targeted high-resolution structure from motion observations over the M 6.4 and M 7.1 ruptures of the Ridgecrest earthquake sequence, *Seismol. Res. Lett.* **91**, no. 4, 2087–2095, doi: [10.1785/0220190274](https://doi.org/10.1785/0220190274).
- DuRoss, C. B., R. D. Gold, T. E. Dawson, K. M. Scherer, K. J. Kendrick, S. O. Akciz, S. J. Angster, J. Bachhuber, S. Bacon, S. E. K. Bennett, et al. (2020). Surface displacement distributions for the July 2019 ridgecrest, California, earthquake ruptures, *Bull. Seismol. Soc. Am.* **110**, 1400–1418, doi: [10.1785/0120200058](https://doi.org/10.1785/0120200058).
- Fault Displacement Hazard Initiative (FDHI) (2018). Fault displacement hazard initiative, available at <https://www.risksciences.ucla.edu/nhr3/fdhi/home> and <https://www.risksciences.ucla.edu/nhr3/fdhi/databases> (last accessed March 2021).

- Fernandez-Diaz, J. C., W. E. Carter, C. Glennie, R. L. Shrestha, Z. Pan, N. Ekhtari, A. Singhania, D. Hauser, and M. Sartori (2016). Capability assessment and performance metrics for the Titan multi-spectral mapping lidar, *Rem. Sens.* **8**, 936, doi: [10.3390/rs8110936](https://doi.org/10.3390/rs8110936).
- Geotechnical Extreme Events Reconnaissance (GEER) (2019). Preliminary report on engineering and geological effects of the July 2019 Ridgecrest Earthquake sequence, *Geotechnical Extreme Events Reconnaissance Association Rep. GEER-064*, doi: [10.18118/G6H66](https://doi.org/10.18118/G6H66).
- Gilbert, G. K. (2010). *The Investigation of the San Francisco Earthquake (1906)*, Kessinger Publishing, 24 pp.
- Goulet, C. A., S. Ahdi, X. Meng, M. Hudson, K. Hudson, and Y. Wang (2021). SCEC field reconnaissance, Ridgecrest, CA Earthquake Sequence, July 4 and 5, 2019, Fault Displacement Feature Interpretation, DesignSafe-CI, doi: [10.17603/ds2-20wf-pz91](https://doi.org/10.17603/ds2-20wf-pz91).
- Haala, N., M. Cramer, and M. Rothermel (2013). Quality of 3d point clouds from highly overlapping Uav imagery, *Int. Arch. Photogramm. Rem. Sens. Spat. Inf. Sci.* **XL-1/W2**, no. August, 183–188.
- Hauksson, E., L. M. Jones, K. Hutton, and D. Eberhart-Phillips (1993). The 1992 Landers earthquake sequence: Seismological observations, *J. Geophys. Res.* **98**, no. B11, 19,835–19,858.
- Hudnut, K. W., B. A. Brooks, K. Scharer, J. L. Hernandez, T. E. Dawson, M. E. Osokin, J. R. Arrowsmith, C. A. Goulet, K. Blake, M. L. Boggs, et al. (2020). Airborne lidar and electro-optical imagery along surface ruptures of the 2019 Ridgecrest earthquake sequence, Southern California, *Seismol. Res. Lett.* **91**, no. 4, 2096–2107, doi: [10.1785/0220190338](https://doi.org/10.1785/0220190338).
- Johri, M., M. D. Zoback, and P. Hennings (2014). A scaling law to characterize fault-damage zones at reservoir depths, *AAPG Bull.* **98**, no. 10, 2057–2079, doi: [10.1306/05061413173](https://doi.org/10.1306/05061413173).
- Milliner, C. W. D., J. F. Dolan, J. Hollingsworth, S. Leprince, and F. Ayoub (2016). Comparison of coseismic near-field and off-fault surface deformation patterns of the 1992 M-w 7.3 Landers and 1999 M-w 7.1 Hector Mine earthquakes: Implications for controls on the distribution of surface strain, *Geophys. Res. Lett.* **43**, 10,115–10,124.
- Milliner, C. W. D., J. F. Dolan, J. Hollingsworth, S. Leprince, F. Ayoub, and C. G. Sammis (2015). Quantifying near-field and off-fault deformation patterns of the 1992 M-w 7.3 Landers earthquake, *Geochem. Geophys. Geosys.* **16**, 1577–1598.
- Moss, R. E. S., and Z. E. Ross (2011). Probabilistic fault displacement hazard analysis for reverse faults, *Bull. Seismol. Soc. Am.* **101**, 1542–1553.
- Mulholland, C. (1894). The Owens valley earthquake of 1872, *Annu. Publ. Hist. Soc. South. Calif., Los Angel.* **3**, no. 2, 27–32.
- Peacock, D. C. P., C. W. Nixon, A. Rotevatn, D. J. Sanderson, and L. F. Zuluaga (2016). Glossary of fault and other fracture networks, *J. Struct. Geol.* **92**, 12–29.
- Petersen, M. D., T. E. Dawson, R. Chen, T. Q. Cao, C. J. Wills, D. P. Schwartz, and A. D. Frankel (2011). Fault displacement hazard for strike-slip faults, *Bull. Seismol. Soc. Am.* **101**, 805–825.
- Ponti, D. J., J. K. Blair, C. M. Rosa, K. Thomas, A. J. Pickering, S. Akciz, S. Angster, J.-P. Avouac, J. Bachhuber, S. Bacon, et al. (2020). Documentation of surface fault rupture and ground deformation features produced by the Ridgecrest M 6.4 and M 7.1 earthquake sequence of July 4 and 5, 2019, *Seismol. Res. Lett.* **91**, no. 5, 2942–2959.
- Power, W. L., and T. E. Tullis (1991). Euclidean and fractal models for the description of rock surface-roughness, *J. Geophys. Res.* **96**, 415–424.
- Rathje, E. M., C. Dawson, J. E. Padgett, J.-P. Pinelli, D. Stanzione, A. Adair, P. Arduino, S. J. Brandenberg, T. Cockerill, M. Esteva, et al. (2017). DesignSafe: A new cyberinfrastructure for natural hazards engineering, *Nat. Hazards Rev.* **18**, no. 3, doi: [10.1061/\(ASCE\)NH.1527-6996.0000246](https://doi.org/10.1061/(ASCE)NH.1527-6996.0000246).
- Rockwell, T. K., S. Lindvall, T. Dawson, R. Langridge, W. Letts, and Y. Klinger (2002). Lateral offsets on surveyed cultural features resulting from the 1999 Izmit and Düzce earthquakes, Turkey, *Bull. Seismol. Soc. Am.* **92**, no. 1, 79–94, doi: [10.1785/0120000809](https://doi.org/10.1785/0120000809).
- Roten, D., K. B. Olsen, and S. M. Day (2017). Off-fault deformations and shallow slip deficit from dynamic rupture simulations with fault zone plasticity, *Geophys. Res. Lett.* **44**, 7733–7742.
- Sagy, A., and E. E. Brodsky (2009). Geometric and rheological asperities in an exposed fault zone, *J. Geophys. Res.* **114**, doi: [10.1029/2008JB005701](https://doi.org/10.1029/2008JB005701).
- Sarmiento, A., N. Abrahamson, S. Baize, Y. Bozorgnia, R. Chen, K. J. Coppersmith, T. Dawson, J. Donahue, V. Jacob, M. Ketabdar, et al. (2019). A new model database for next-generation fault displacement hazard analysis, *Seismological Society of America Annual Meeting*, Seattle, Washington, 23–26 April 2019.
- Sauber, J., W. Thatcher, S. C. Solomon, and M. Lisowski (1994). Geodetic slip rate for the eastern California shear zone and the recurrence time of Mojave Desert earthquakes, *Nature* **367**, no. 6460, 264–266.
- Stepp, J. C., I. Wong, J. Whitney, R. Quittmeyer, N. Abrahamson, G. Toro, R. Youngs, K. Coppersmith, J. Savoy, T. Sullivan, et al. (2001). Probabilistic seismic hazard analyses for ground motions and fault displacement at Yucca Mountain, Nevada, *Earthq. Spectra* **17**, 113–151.
- Thomas, M. Y., and H. S. Bhat (2018). Dynamic evolution of off-fault medium during an earthquake: A micromechanics based model, *Geophys. J. Int.* **214**, no. 2, 1267–1280, doi: [10.1093/gji/ggy129](https://doi.org/10.1093/gji/ggy129).
- Treiman, J. A., K. J. Kendrick, W. A. Bryant, T. K. Rockwell, and S. F. McGill (2002). Primary surface rupture associated with the  $M_w$  7.1 16 October 1999 Hector Mine earthquake, San Bernardino County, California, *Bull. Seismol. Soc. Am.* **92**, no. 4, 1171–1191, doi: [10.1785/0120000923](https://doi.org/10.1785/0120000923).
- Vermilye, J. M., and C. H. Scholz (1998). The process zone: A microstructural view of fault growth, *J. Geophys. Res.* **103**, no. B6, 12,223–12,237, doi: [10.1029/98JB00957](https://doi.org/10.1029/98JB00957).
- Wang, Y., and C. Goulet (2021). Validation of fault displacements from dynamic rupture simulations against the observations from the 1992 landers earthquake, *Bull. Seismol. Soc. Am.* 1–21, doi: [10.1785/0120210082](https://doi.org/10.1785/0120210082).
- Youngs, R. R., W. J. Arabasz, R. E. Anderson, A. R. Ramelli, J. P. Ake, D. B. Slemmons, J. P. McCalpin, D. I. Doser, C. J. Fridrich, F. H. Swan, et al. (2003). A methodology for probabilistic fault displacement hazard analysis (PFDHA), *Earthq. Spectra* **19**, 191–219.

Manuscript received 22 June 2020  
Published online 24 August 2021